

# Airborne in-situ quantification of methane emissions from oil and gas production in Romania

Hossein Maazallahi<sup>1,2,\*</sup>, Foteini Stavropoulou<sup>1,3</sup>, Samuel Jonson Sutanto<sup>1,\*\*</sup>, Michael Steiner<sup>4</sup>, Dominik Brunner<sup>4,5</sup>, Mariano Mertens<sup>6</sup>, Patrick Jöckel<sup>6</sup>, Antoon Visschedijk<sup>2</sup>, Hugo Denier van der Gon<sup>2</sup>, Stijn Dellaert<sup>2</sup>, Nataly Velandia Salinas<sup>3</sup>, Stefan Schwietzke<sup>3</sup>, Daniel Zavala Araiza<sup>3</sup>, Sorin Ghemulet<sup>7</sup>, Alexandru Pana<sup>7</sup>, Magdalena Ardelean<sup>7</sup>, Marius Corbu<sup>7</sup>, Andreea Calcan<sup>7</sup>, Stephen A. Conley<sup>8</sup>, Mackenzie L. Smith<sup>8</sup>, Thomas Röckmann<sup>1</sup>

<sup>1</sup> Institute for Marine and Atmospheric research Utrecht (IMAU), Utrecht University, Utrecht, the Netherlands

<sup>2</sup> Netherlands Organisation for Applied Scientific Research (TNO), Utrecht, the Netherlands

<sup>3</sup> Environmental Defense Fund (EDF), Berlin, Germany, and Amsterdam, the Netherlands

<sup>4</sup> Laboratory for Air Pollution/Environmental Technology, Empa - Swiss Federal Laboratories for Materials Science and Technology, Dübendorf, Switzerland

<sup>5</sup> Institute for Atmospheric and Climate Science, ETH Zurich, Zurich, Switzerland

<sup>6</sup> Deutsches Zentrum für Luft- und Raumfahrt, Institut für Physik der Atmosphäre, Oberpfaffenhofen, Germany

<sup>7</sup> National Institute for Aerospace Research “Elie Carafoli” (INCAS), Bucharest, Romania

<sup>8</sup> Scientific Aviation (SA), Inc., 3335 Airport Road Suite B, Boulder, Colorado 80301, United States

\* Now at: Department of Renewable Energies and Environment, College of Interdisciplinary Science and Technologies, University of Tehran, Tehran, Iran.

\*\* Now at: Earth Systems and Global Change, Wageningen University and Research, Wageningen, the Netherlands.

## Correspondence to:

Hossein Maazallahi ([h.maazallahi@ut.ac.ir](mailto:h.maazallahi@ut.ac.ir)), Thomas Röckmann ([t.roeckmann@uu.nl](mailto:t.roeckmann@uu.nl))

## Abstract

Production of oil and gas in Romania, one of the largest producers in the EU, is associated with substantial emissions of methane to the atmosphere and may offer high emission mitigation potential to reach the climate objectives of the EU. However, comprehensive quantification of emissions in this area has been lacking. Here we report top-down emission rate estimates derived from aircraft-based in-situ measurements that were carried out with two aircraft during the ROMEO 2019 campaign, supported by simulations with atmospheric models. Estimates from mass balance flights at individual dense production clusters, and around larger regions, show large variations between the clusters, supporting the important role of individual super emitters, and possibly variable operation practices or maintenance state across the production basin. Estimated annual total emissions from the Southern Romanian Oil and Gas (O&G) infrastructure are  $227 \pm 86$  kt CH<sub>4</sub> yr<sup>-1</sup>, consistent with previously published estimates from ground-based site-level measurements during the same period. The comparison of individual plumes between measurements and atmospheric model simulations was complicated by

41 unfavorable low wind conditions. Similar correlations between measured and simulated CH<sub>4</sub>  
42 enhancements during large-scale raster flights and mass balance flights suggest that the  
43 emission factor determined from a limited number of production clusters is representative for  
44 the larger regions. We conclude that ground-based and aerial emission rate estimates derived  
45 from the ROMEO campaign agree well, and the aircraft observations support the previously  
46 suggested large under-reporting of CH<sub>4</sub> emissions from the Romanian O&G industry in 2019  
47 to United Nations Framework Convention on Climate Change (UNFCCC). We also observed  
48 large underestimation from O&G emissions in the Emissions Database for Global Atmospheric  
49 Research (EDGAR) v7.0 for our domain of study.

## 50 **1. Introduction**

51 Methane (CH<sub>4</sub>) is a potent greenhouse gas with more than 80 times the global warming  
52 potential of carbon dioxide (CO<sub>2</sub>) over a 20-year time horizon (Szopa et al., 2021).  
53 Approximately, 60% of global CH<sub>4</sub> emissions are attributed to human activities, with roughly  
54 one-third of them resulting from the Oil and Gas (O&G) industry (Saunio et al., 2020).  
55 Reducing CH<sub>4</sub> emissions from the O&G industry presents an easily accessible and cost-  
56 effective mitigation option (Shindell et al., 2021). Given the relatively short lifetime of CH<sub>4</sub> in  
57 the atmosphere ( $\approx 10$  years), such measures would lead to substantial climate benefits in both  
58 the near- and long-term future (Shindell et al., 2021;Collins et al., 2018). Scenarios that are  
59 compatible with the goal of the Paris Agreement (UNFCCC, 2015) to limit global warming to  
60 2 °C, preferentially to 1.5 °C all include substantial reductions in CH<sub>4</sub>, and the current growth  
61 in CH<sub>4</sub> is incompatible with reaching this goal (Nisbet et al., 2020).

62 Improving our understanding of CH<sub>4</sub> emissions from the O&G industry requires  
63 comprehensive and accurate emission measurements using a combination of approaches.  
64 Several studies, mostly in North America, consistently show that national inventories, which  
65 rely on multiplying activity data with generic emission factors, tend to underestimate CH<sub>4</sub>  
66 emissions from the O&G industry (Allen et al., 2013;Brandt et al., 2014;Harriss et al.,  
67 2015;Johnson et al., 2017;Alvarez et al., 2018;Weller et al., 2020).

68 CH<sub>4</sub> emissions can be quantified using top-down or bottom-up approaches. Top-down  
69 approaches use ambient CH<sub>4</sub> mole fraction measurements from aircraft, tall towers, weather  
70 stations or satellites, combined with models to estimate the total CH<sub>4</sub> flux rate at different scales  
71 (i.e., site-level to regional or country-level). These approaches ensure that emissions from all  
72 sources are captured. Other techniques, such as the use of ethane (C<sub>2</sub>H<sub>6</sub>) and the isotopic  
73 composition of CH<sub>4</sub> as tracers, can help attribute CH<sub>4</sub> emissions to O&G industry or other  
74 sectors (Röckmann et al., 2016;Lopez et al., 2017;Mielke-Maday et al., 2019;Maazallahi et al.,  
75 2020;Lu et al., 2021;Menoud et al., 2021;Gonzalez Moguel et al., 2022;Fernandez et al., 2022).  
76 Bottom-up approaches involve direct measurements of emissions usually at the source or  
77 component-level which are then extrapolated to larger scales using statistical methods.

78 The emission data reported to the United Nations Framework Convention on Climate  
79 Change (UNFCCC) for the year 2021 reveal that Romania ranks among the European Union  
80 (EU) countries with the highest annual CH<sub>4</sub> emissions from the O&G activities, following  
81 closely behind Italy and Poland. The International Energy Agency (IEA) estimates that  
82 Romania contributes the highest CH<sub>4</sub> emissions from the O&G industry among the EU-27  
83 countries (IEA, 2023). In light of the recent provisional agreement of EU methane regulations,  
84 which impose new requirements on the O&G industry for measuring, reporting, and mitigating  
85 CH<sub>4</sub> emissions (European-Commission, 2023), there is an urgent need to understand the extent  
86 and magnitude of emissions. This is particularly relevant for countries like Romania, where  
87 emissions are substantial but understudied, and addressing them is crucial for achieving EU  
88 climate objectives.

89 The ROMEO (ROmanian Methane Emissions from Oil and gas) project was designed  
90 to provide independent scientific measurement based CH<sub>4</sub> emission estimates for the O&G  
91 producing regions in Romania (Stavropoulou et al., 2023). The first phase of the ROMEO  
92 campaign took place in October 2019, covering large production areas in southern Romania  
93 that are mostly associated with oil production. The second phase happened in the following  
94 year and focused on the gas production region in the Transylvanian Basin, north of the  
95 mountain range. Numerous measurement techniques using a variety of instruments were  
96 deployed onboard ground-based and airborne measurement platforms. The data collected by  
97 vehicles and UAVs during the ROMEO campaign have already been evaluated separately in  
98 prior studies (Stavropoulou et al., 2023; Delre et al., 2022; Korbeń et al., 2022). Additionally,  
99 Menoud et al. (2022) investigated the isotopic signature of CH<sub>4</sub> emissions from the sites visited  
100 during the ROMEO campaign, contributing to insights in the reservoir characteristics.

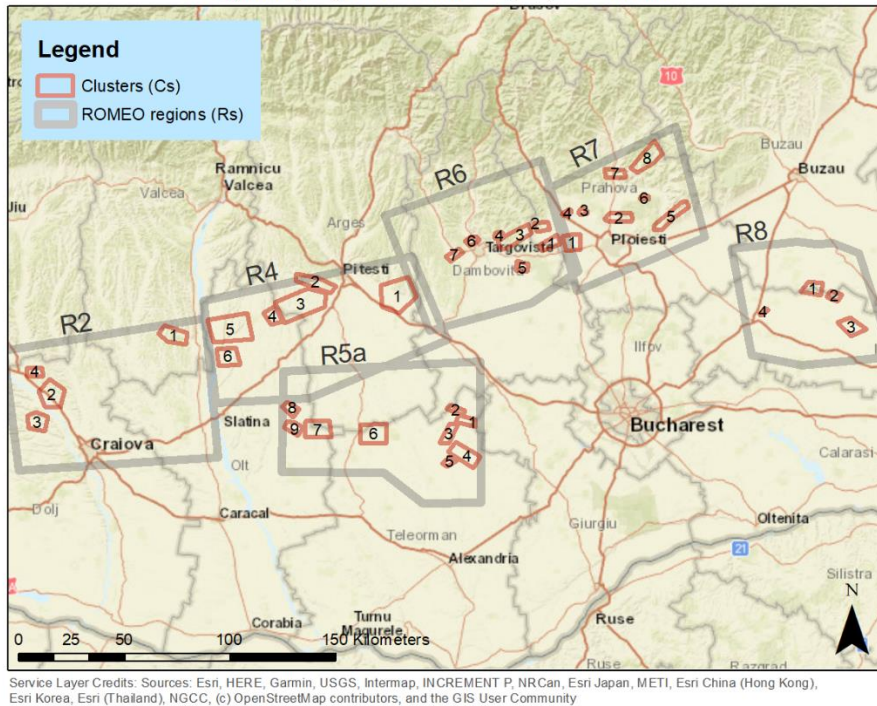
101 In this study, we present top-down CH<sub>4</sub> emission estimates derived from aircraft  
102 measurements of individual facilities, facility clusters, and extended regions during the  
103 ROMEO campaign. The measurements were performed by two research aircraft, and we used  
104 two mesoscale atmospheric chemistry and transport models to simulate atmospheric  
105 composition and transport over Romania.

## 106 **2. Materials and methods**

### 107 **2.1. Clusters and regions**

108 Information of O&G activities including locations, production asset types, status and  
109 age of the facilities were received from the largest operator in the region. This information  
110 covers the majority of the sites in the survey region, though other smaller operators are also  
111 present. The distribution of O&G production infrastructure in Romania is heterogeneous with  
112 a high density of production sites concentrated above the subsurface fossil fuel reservoirs.  
113 Therefore, we first grouped the installations in 40 clusters (Cs) and regions (Rs) (i.e.,  
114 aggregation of several production clusters) (Fig. 1). Both production clusters and regions were  
115 targets for the quantification approaches in the ROMEO campaign. Clusters are relatively small  
116 areas, usually a few to 20 km<sup>2</sup>, with a high density of O&G production sites. To derive basin-  
117 scale emission rates from aircraft measurements, the Romanian plain was further divided into  
118 larger regions of roughly 50 x 50 km<sup>2</sup>, which contain the clusters and are suitable for aircraft  
119 mass balance and raster flights.

Regions (Rs) and Clusters (Cs) Boundaries



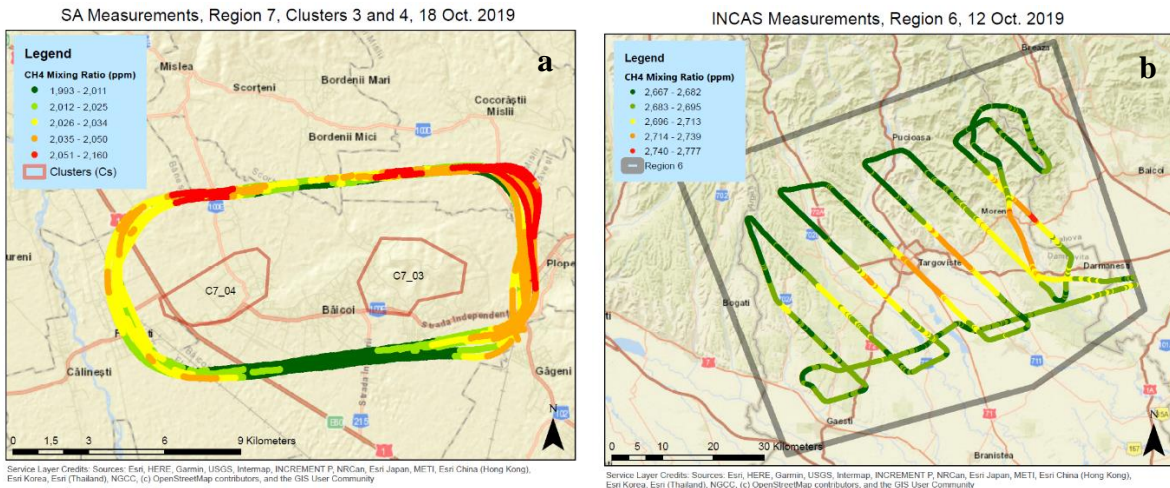
120

121 *Figure 1. Regions (grey polygons) and clusters (red polygons) that were targeted during the*  
 122 *ROMEIO 2019 campaign, circular or raster flights were performed within or around these*  
 123 *boundaries.*

124 **2.2. Aircraft-based in situ measurements**

125 Two aircraft were deployed during the ROMEIO 2019 campaign, a BN2 aircraft  
 126 operated by the National Institute for Aerospace Research "Elie Carafoli" (INCAS) and a two-  
 127 seater Mooney aircraft operated by Scientific Aviation (SA) Inc. On the Mooney aircraft, in-  
 128 situ measurements of CH<sub>4</sub>, C<sub>2</sub>H<sub>6</sub>, carbon dioxide (CO<sub>2</sub>), wind speed and direction, and relative  
 129 humidity were continuously logged at 1Hz frequency. C<sub>2</sub>H<sub>6</sub> and CO<sub>2</sub> were measured with  
 130 AERIS Pico Mobile LDS and Picarro G2301-f instruments and both instruments measured CH<sub>4</sub>  
 131 individually. On the BN2 aircraft, CH<sub>4</sub>, CO<sub>2</sub> and carbon monoxide (CO) were measured at  
 132 about 0.3 Hz frequency using a G2401 analyzer (Picarro Inc).

133 Two sets of flight patterns were performed, mass balance flights circling around target  
 134 areas (Fig. 2, left) and raster flights scanning the areas at a pre-selected observation density  
 135 (Fig. 2, right). During the 18 individual mass balance flights with the SA aircraft, the target  
 136 emission locations were circled at different altitudes to map the extent of the emission plume  
 137 (s), both vertically and horizontally. The emission rates were then calculated from the  
 138 measurements of CH<sub>4</sub> mole fraction and wind speed and direction in the mass balance approach  
 139 (see below). The BN2 aircraft was used to map possible emission sources over more extended  
 140 areas. The lack of wind measurements from this aircraft precludes a direct emission  
 141 quantification using the mass balance approach. These extended areas were surveyed in raster  
 142 patterns perpendicular to the prevailing wind (Fig. 2b). In addition to the identification of larger  
 143 sources, these measurements are also used to derive indirect emission rate estimates by  
 144 comparison to model simulations (see below).



146  
 147 *Figure 2 – Examples of a mass balance flight, south wind from measurements (a) and a raster*  
 148 *flight with east-east-north from simulations (b) during the ROMEO 2019 campaign. The mass*  
 149 *balance flight circled around two production clusters located in close proximity and the raster*  
 150 *flight covers a larger region. The color scale represents the CH<sub>4</sub> mole fraction.*

### 151 2.3. Model simulations

152 In order to support the emission quantification from the aircraft measurements, we  
 153 simulated atmospheric composition and transport over Romania using two numerical mesoscale  
 154 atmospheric chemistry and transport models: COSMO-GHG operated by the Swiss Federal  
 155 Laboratories for Materials Science and Technology (EMPA) and MECO(n) operated by the  
 156 German Aerospace Center (DLR). COSMO-GHG is based on the regional numerical weather  
 157 prediction and climate model COSMO-CLM (Baldauf et al., 2011) and includes the GHG  
 158 extension (Jähn et al., 2020; Brunner et al., 2019) for the simulation of (nearly) passive trace  
 159 gases such as CH<sub>4</sub>. MECO(n) features an on-line coupling of the global chemistry-climate  
 160 model EMAC with the regional chemistry-climate model COSMO-CLM/MESSy (Kerkweg  
 161 and Jöckel, 2012). The COSMO-GHG simulations were nudged to the hourly wind data from  
 162 the ERA5 reanalysis product of the European Centre for Medium-Range Weather Forecasts  
 163 (ECMWF) (Hersbach et al., 2023). In MECO(n) the global model (EMAC) was nudged by  
 164 Newtonian relaxation towards the operational analysis data from ECMWF (see (Nickl et al.,  
 165 2020) for more details).

166 These two models were used to simulate the evolution of the CH<sub>4</sub> mole fraction arising  
 167 from emissions from active O&G assets, including individual wells and larger facilities in time  
 168 and space. For setting up the model simulations, each site was assigned an emission rate of 1 g  
 169 s<sup>-1</sup> (3.6 kg hr<sup>-1</sup>). For COSMO-GHG, the model resolution was 2 x 2 km<sup>2</sup>, and the meteorological  
 170 and compositional boundary conditions were provided from global scale modeling results  
 171 obtained with the ECMWF/CAMS system. The MECO(n=3) set-up comprised four model  
 172 instances (see Klausner et al. (2020) for a detailed description of a similar model set-up). The  
 173 first is the global model instance EMAC with a resolution of T42L90MA (corresponding to  
 174 around 280 km spatial resolution). In the global model, three COSMO-CLM/MESSy instances  
 175 were nested on-line with approx. 50 km resolution, approx. 7 km resolution, and the same 2 x  
 176 2 km domain as applied for COSMO-GHG, respectively. In the applied MECO(3) set-up, we  
 177 used a parameterized chemistry of methane (Winterstein and Jöckel, 2021) with monthly mean  
 178 OH fields from previous simulations with comprehensive interactive chemistry. In the first,  
 179 second, and third MECO(3) model instance, we prescribed all anthropogenic and natural  
 180 emissions of methane, in order to achieve realistic boundary conditions of methane for the finest

181 resolved instance. In this instance the emissions were used as described below. The model  
182 outputs provide atmospheric CH<sub>4</sub> mole fractions fields as well as meteorological parameters at  
183 a temporal resolution of 20 min (COSMO-GHG) and 1 hr (MECO(3)). For MECO(3), only the  
184 results of the finest instance are considered here for further analysis. To be able to geo-attribute  
185 emissions to certain emission clusters, we applied 33 individual model-based prognostic CH<sub>4</sub>  
186 tracers in the models which are transported according to the meteorological conditions. Each of  
187 these tracers represents the emissions of a specific area with a fixed emission rate of 1 g s<sup>-1</sup> or  
188 3.6 kg hr<sup>-1</sup> and released at one individual or multiple release point(s). Meaning that one tracer  
189 represents the emissions of one or two clusters and one or two distant regions, assuming that  
190 they are sufficiently far away. This allows us to separate the signal of each cluster / region flown  
191 over or circled around. During the analysis, these tracers are not further considered, because,  
192 since the attribution by location is usually unambiguous.

## 193 **2.4. Emission inventories**

194 To drive the simulations and interpret the data we use information from various  
195 emission inventories. (I) The most granular dataset is based on information on the production  
196 infrastructure provided by the oil and gas operator. It consists of about 6000 individual  
197 production-related locations in the Southern part of Romania. We will refer to this dataset as  
198 the “O&G\_operator” dataset. In order to convert this to an approximate emission inventory, we  
199 divided reported emissions for Romania by the number of emission locations and assigned the  
200 result as average emission rate to all of these locations. Coincidentally, this average value is  
201 close to 1 g s<sup>-1</sup> site<sup>-1</sup> (3.6 kg hr<sup>-1</sup> site<sup>-1</sup>), which was used as prior emission rate in the model  
202 simulations. (II) The TNO\_GHGco inventory (Denier van der Gon et al., 2018) includes  
203 emissions from all available sectors at 5 km x 5 km resolution. (III) The European Pollutant  
204 Release and Transfer Register/Industrial Emissions Directive (E-PRTR/IED) inventory (E-  
205 PRTR, 2023) includes major point sources and was used to identify major farm and landfill  
206 methane emitters within the study areas (Figure S2 in the SI). (IV) The TNO - Copernicus  
207 Atmospheric Monitoring Service European Regional Inventory (TNO-CAMS) v6.0 (Kuenen et  
208 al., 2022) and (V) the Emissions Database for Global Atmospheric Research (EDGAR, 2023)  
209 v7.0 inventories were both used to calculate the percentage of O&G emissions to total emissions  
210 in the target areas.

211 In summary, based on TNO-CAMS no coal mine locations, a potentially large source  
212 of CH<sub>4</sub>, were identified within the mass balance flight boundaries. The presence of major  
213 wetlands was investigated based on the findings of Saarnio et al. (2009) and no wetlands were  
214 observed within the measured areas.

## 215 **2.5. Analysis of simulated meteorological quantities**

216 The meteorological conditions during the ROMEO campaign were not ideal for  
217 emission quantification due to the low wind speeds. This complicated the use of a model –  
218 measurement comparison for the raster flights, which we had planned to use to derive  
219 quantitative emission information. To assess the model performance in terms of meteorological  
220 conditions during the individual flight days, we compared the meteorological output of the  
221 models with each other, with ERA5 reanalysis data, and with the meteorological information  
222 recorded during the Scientific Aviation flights. The rationale is: when the models do not agree  
223 on the general meteorological conditions in a target region, we also expect diverging CH<sub>4</sub>  
224 concentration distributions, which would hamper quantitative comparison to the measurements.  
225 On the other hand, when the meteorological conditions are simulated consistently, there is more  
226 confidence that the transport is simulated adequately as well, thus the simulated and observed  
227 CH<sub>4</sub> plumes may be used to derive emission information.

228 For each flight date, the following parameters were investigated in each flight region:  
 229 temperature, cloud fraction, wind speed and direction, specific humidity, and relative humidity.  
 230 Based on selected threshold values, the meteorological parameters for each model and each  
 231 flight day were characterized as good, acceptable, or poor. Furthermore, we evaluate three  
 232 quantitative indices, the Nash - Sutcliffe Efficiency (NSE), the Kling-Gupta Efficiency (KGE),  
 233 and the Mean Absolute Relative Error (MARE) between simulation results and ERA5  
 234 reanalysis data. The results of this comprehensive analysis are presented in the Supplementary  
 235 Information (SI) S.1.

## 236 **2.6. Emission quantification: Mass balance approach**

237 CH<sub>4</sub> emission rates from 11 production site clusters (or combinations of clusters), three  
 238 larger regions in the Romanian Basin, and two groups of individual sites were quantified from  
 239 aircraft-based measurements using the mass balance approach. This approach is based on the  
 240 Gaussian theorem in which the difference of the total fluxes into and out of an enclosed area  
 241 must be balanced by a source or sink in the area (Conley et al., 2017). CH<sub>4</sub> enhancements were  
 242 identified using background values determined either from the upwind flight legs or from the  
 243 edges of detected plumes.

244 The mass balance approach returns total CH<sub>4</sub> emissions for the target areas. For the  
 245 intense production clusters, the emissions are in most cases dominated by the O&G production  
 246 infrastructure. Therefore, we assigned 100% of the emissions in the clusters to O&G  
 247 production, except for clusters which contained a landfill and/or large farm, as included in the  
 248 E-PRTR inventory. In particular, only one significant landfill was identified in R6C6, and the  
 249 emissions reported from this landfill were deducted from the measured flight quantification.  
 250 For the larger areas, the contributions from other sectors can be substantial. To infer emissions  
 251 related to O&G operations from the total measured emissions, we estimated the emissions from  
 252 non-O&G sources in the target areas using the TNO-CAMS inventory and subtracted these  
 253 from the total measured emissions. We repeated the same process using the EDGAR v7.0  
 254 inventory. These O&G related emissions were then divided by the number of active O&G  
 255 infrastructure elements in the target area to derive an emission factor per site for that cluster or  
 256 region. This includes active production sites, processing sites, compressor stations, and other  
 257 active sites, which all contribute to the measured emissions. Possible emissions of non-  
 258 producing sites are not included in our estimates, as they are likely smaller (on average) than  
 259 the ones of producing sites.

## 260 **2.7. Emission quantification: Measurement - model comparison**

### 261 **2.7.1. Mass balance flights**

262 Equation 1 was used to translate the aircraft measurements into the emission rates which  
 263 is described in detail by Conley et al. (2017).

$$264 \quad Q_c = \left\langle \frac{\partial m}{\partial t} \right\rangle + \int_0^{z^{\max}} \oint c' u_h \cdot \hat{n} \, dl dz \quad \text{Eq. 1}$$

265 Here,  $Q_c$  is the net emission from source (s) and sink (s),  $l$  is the position along the flight  
 266 path,  $\hat{n}$  is the a vector normal to surface pointing outward,  $u_h (= u_i + v_j)$ ,  $c'$  is the CH<sub>4</sub>  
 267 enhancement from the mean of each circle's mixing ratio and  $\left\langle \frac{\partial m}{\partial t} \right\rangle$  is the total mass trend  
 268 within the volume of each box.

269 The simulated CH<sub>4</sub> distributions were evaluated along the flight tracks in order to  
 270 facilitate direct comparison with the observations. For the mass balance flights (Fig 2a), the  
 271 lowest CH<sub>4</sub> value of each circle around a target area retrieved from the Picarro instrument was  
 272 defined as background mole fraction and subtracted from downwind measurements to obtain  
 273 the CH<sub>4</sub> enhancement. To compare model and measurement results, we integrated the CH<sub>4</sub>

274 enhancement above background along the flight track for each circle, both for the measurements  
275 and for the simulated CH<sub>4</sub> mole fractions along the flight tracks. These integrals are referred to  
276 as plume areas. Circles that were identified as influenced by up-stream contamination were  
277 excluded from the analysis. The simulated plume areas were then plotted versus the measured  
278 plume areas, and the slope of the orthogonal linear regression line returns a measurement-based  
279 scaling factor to the prior emission rate estimate that was in the simulations (1 g s<sup>-1</sup> site<sup>-1</sup>). This  
280 scaling factor was then assigned to the active O&G facilities in the target cluster or region and  
281 provides a measurement-based estimate of the emission factor.

## 282 **2.7.2. Raster flights**

283 For the raster flights (Fig. 2b), the lowest CH<sub>4</sub> mole fraction along the flight track across  
284 a target region was defined as background and the CH<sub>4</sub> enhancements above this background  
285 were integrated. The simulations were treated in the same way. The slopes of the orthogonal  
286 linear regressions between integrated enhancements from flight measurements and simulations  
287 were then compared to the scaling factors determined from the mass balance flights (2.7.1) to  
288 investigate whether the model – observation slopes are consistent between individual plumes  
289 and the raster flights over larger regions. The rationale is that even if the quantitative modeling  
290 is challenging under the encountered meteorological conditions, if the slopes derived from the  
291 mass balance and raster flights are comparable, then the emission factors derived from the mass  
292 balance flights should be also representative for the larger regions covered by the raster flights.

## 293 **3. Results and discussion**

### 294 **3.1. Mass balance quantifications**

295 Table 1 shows the results of the emission quantifications obtained from mass balance  
296 calculations using the measurements of the SA aircraft. Methane emission rates range between  
297 tens of kg hr<sup>-1</sup> from an individual facility or smaller cluster up to more than 8000 kg hr<sup>-1</sup> for the  
298 larger region R7 which includes the city of Ploiesti (Fig. 1). These emissions are representative  
299 of the sum of all sources in each target area. Especially the larger regions include emissions  
300 from other sectors, particularly agriculture and waste. On the other hand, the CH<sub>4</sub> in the dense  
301 production clusters originate nearly 100% from O&G activities.

302 Different inventories (E-PRTR, TNO-CAMS v6.0, and EDGAR v7.0) were consulted  
303 to obtain information about the non-O&G contributions; however, these inventories are  
304 generally not designed to distribute emissions across sectors on such small scales. TNO-CAMS  
305 and EDGAR have a coarse spatial resolution and do not include production clusters, so they are  
306 not suitable to assess the emissions distribution across sectors in such clusters. With the  
307 exception of R6C6, which includes a landfill listed in E-PRTR for the year 2019, for all other  
308 production clusters, E-PRTR does not indicate any major farms or landfills. The ground teams  
309 did not observe significant non-O&G sources in the smaller production clusters. Therefore, we  
310 ascribe 100% of the total emissions in clusters to O&G production. For the large regions R7  
311 and R5a, we use the estimated absolute non-O&G emissions from TNO-CAMS and subtract  
312 them from the measured emissions to correct for non-O&G related emissions.

313 The emission factors (EF) provided in Table 1 are calculated using the number of total  
314 active (e.g. producing, or operating) infrastructure elements within the target regions, because  
315 the measurements do not allow us to distinguish between different parts of the infrastructure.  
316 The emission factors vary widely among the individual clusters, from 1.0 to 20 kg hr<sup>-1</sup> site<sup>-1</sup>.  
317 This is partly due to the inhomogeneous distribution of the emissions, where few sites are  
318 responsible for a large share of the emissions. A contributing factor is that each quantification  
319 yields an emission estimate for the specific moment in time of the measurement. The variability  
320 in our cluster-specific emission factors may partly represent the episodic tendency of O&G



321 super-emitters. However, given the generally large number of infrastructure elements within  
322 the target regions, the reported numbers should still reflect representative averages for the  
323 clusters and regions, also over longer periods. Note that the timing of our measurements is  
324 random, and the total facility sample size ( $N=4358$ , including duplicates, see below) is large.  
325 To address the challenge of emissions' variability and inhomogeneity, we employ a weighted  
326 averaging approach based on facility numbers.

327 The sum of all emissions from the airborne  $\text{CH}_4$  emission measurements (SA01-SA18)  
328 from all flights reach  $31,700 \text{ kg hr}^{-1}$  accounting for 4358 active sites measured during all flights  
329 combined (Table 1). This results in EF of  $7.3 \text{ kg hr}^{-1} \text{ site}^{-1}$  after a simple division. However,  
330 this EF is biased for two reasons: (I) not all emissions measured ( $31,700 \text{ kg hr}^{-1}$ ) are from O&G  
331 sources and (II) there are double to triple countings of emissions in total sum, e.g. R5a and R7  
332 is measured twice or three times. The first point results in overestimation of EFs from O&G  
333 activities and the latter point results in biasing the average EF towards emission rates of sources  
334 which were measured more than once. Therefore, we performed several analyses to address  
335 these two points.

336 In total, in addition to cluster-focused flights for R7, two regional flights have been  
337 performed per R7 and R5a each, which results in triple countings of emissions for R7 and  
338 double countings of emissions for R5a in the total sum of  $31,700 \text{ kg hr}^{-1}$ . Hence, we used average  
339 emission rates from the regional measurements targeting the R7 and R5a individually (SA01  
340 and SA02 for R7 and SA03 and SA04 for R5a, respectively). For the regions R4, R6 and R8 no  
341 regional flights were performed, and cluster-focused quantifications were performed. We used  
342 the sum of emissions from these clusters as the total emissions for these regions. These  
343 corrections result in cumulative emissions of  $13,200 \pm 4,932 \text{ kg hr}^{-1}$  for these regions,  
344 accounting for 2516 active sites which results in EF of  $5.3 \pm 2.0 \text{ kg hr}^{-1} \text{ site}^{-1}$ .

345 Acting on the field observations and inventory information, emissions from all clusters  
346 can be assigned to O&G activities except for the R6C6. After deducting reported emissions for  
347 the landfill within the boundary of R6C6 and adding to the measured emissions from other  
348 clusters, we reach total emission of  $6,970 \pm 2,610 \text{ kg hr}^{-1}$  for 1,570 sites which results in EF of  
349 is  $4.4 \pm 1.7 \text{ kg hr}^{-1} \text{ site}^{-1}$ .

350 Both EFs,  $5.3 \pm 2.0 \text{ kg hr}^{-1} \text{ site}^{-1}$  and  $4.4 \pm 1.7 \text{ kg hr}^{-1} \text{ site}^{-1}$ , overlap with the EF of  $5.4$   
351  $\text{kg hr}^{-1}$  (95% CI:  $3.6 - 8.4 \text{ kg hr}^{-1}$ ) oil production site<sup>-1</sup> reported from ground-based  
352 measurements by Stavropoulou et al. (2023). However, both EFs from the airborne  
353 measurements fall on the lower side of the EF from the ground based measurement. This could  
354 be explained as follows: (I) It is assumed in Eq. 1 that all emissions within the flight boundaries  
355 are transported horizontally and captured during the flights. However, during the ROMEO  
356 campaign, the low wind speed condition and high solar radiation could result in vertical  
357 transport, which was not measured during the airborne measurements. It is possible that the  
358 area mass balance quantifications in the flat and arid region R5a in Southern Romania may be  
359 biased slightly low due to partial loss of  $\text{CH}_4$  out of the boundary layer during the hot and  
360 convective conditions, or due to the fact that stable transport conditions had not yet established  
361 over the large regions. (II) The quantifications reported by Stavropoulou et al.(2023) were  
362 focused on the oil production for which gas production, which is mostly methane, is not  
363 favorable, hence released which we could also observe through optical gas imaging cameras.  
364 This release is favorable to happen at the production sites to prevent two-phase conditions in  
365 the pipelines and collection and processing systems. These two reasons individually or  
366 combined could explain this average difference between the EFs derived from airborne and  
367 ground-based measurements. The difference between the two EFs derived from the airborne  
368 measurements,  $5.3 \pm 2.0 \text{ kg hr}^{-1} \text{ site}^{-1}$  from regional measurements and  $4.4 \pm 1.7 \text{ kg hr}^{-1} \text{ site}^{-1}$

369 from the clusters only, could be explained by the presence of large emitters outside the clusters  
370 but within the regional boundaries.

371 As the campaign airport was located close to the city of Ploiesti in region R7, the  
372 majority of cluster quantifications were carried out in R7 for logistical reasons and many of the  
373 dense production clusters in R7 were quantified. This allows us to compare the sum of the  
374 emission rates determined from cluster quantifications to the emission factors from regional  
375 quantifications. The cluster flights in region R7 quantified a total of 377 O&G sites, which is  
376 75% of the 500 sites that were quantified in the regional flights. The quantified emissions from  
377 the cluster flights ( $3,828 \pm 1,199 \text{ kg hr}^{-1}$ ) amount to 54% of the total emissions quantified in the  
378 regional flights, after subtracting non-O&G emissions (about  $7,038 \pm 1,769 \text{ kg hr}^{-1}$  from two  
379 independent flights, Table 1). This indicates a possible underestimate of non-O&G emissions  
380 in the inventories for R7, which includes the large city of Ploiesti. Alternatively, some super-  
381 emitters may exist outside the quantified clusters, which would increase the regional estimate.  
382 Nevertheless, the region and cluster flights show a reasonable level of consistency in region R7.  
383 The emission factors further support this alignment, with the weighted sum of the clusters being  
384 equal to  $10.2 \pm 3.2 \text{ kg hr}^{-1} \text{ site}^{-1}$  compared to about  $14.1 \pm 3.6 \text{ kg hr}^{-1} \text{ site}^{-1}$  for the regional  
385 flights. While the measurement-based quantifications for region R7 from the two flights are  
386  $7,129 \pm 2,097 \text{ kg hr}^{-1}$  and  $6,947 \pm 1,440 \text{ kg hr}^{-1}$ , reported emissions for O&G activities in TNO-  
387 CAMS v6.0 and EDGAR v7.0 for this region were  $3,112 \text{ kg hr}^{-1}$  and  $73 \text{ kg hr}^{-1}$ , respectively.  
388 This shows large difference between inventories and particularly a large underestimation in  
389 EDGAR v7.0 by a factor of about 100. The underestimation of O&G emissions from production  
390 areas in the earlier versions of EDGAR inventory has also been noted previously (Maasackers  
391 et al., 2016; Scarpelli et al., 2020; Sheng et al., 2017). The causes and discrepancies of the  
392 difference observed between the measurements and the inventories require further  
393 investigation, which is beyond the scope of this study.

394 The aircraft-based quantifications indicate that per-site emission factors from region R7  
395 are higher than from the other regions. At the same time, R7 was best covered in terms of mass  
396 balance determinations, so it is the most reliable estimate. From the site-level quantifications  
397 carried out on the ground, it was not apparent that per-site emission rates varied between  
398 different regions (Stavropoulou et al., 2023; Delre et al., 2022; Korbeń et al., 2022).

399 When we use the derived emission factor of  $5.3 \pm 2.0 \text{ kg hr}^{-1} \text{ site}^{-1}$  and scale this up to  
400 the entire production basin in Southern Romania with more than 4,900 active sites, annual  
401 estimated emissions reached at  $227 \pm 86 \text{ kt CH}_4 \text{ yr}^{-1}$ . If the derived EF also applies to the  
402 infrastructure in other parts of Romania the inferred country-scale emission rate from about  
403 7,400 active sites in 2019 is  $344 \pm 130 \text{ kt CH}_4 \text{ yr}^{-1}$ . Reported emissions to the UNFCCC for  
404 Romania in the category *1.B: Fugitives* include  $53 \text{ kt CH}_4 \text{ yr}^{-1}$  for activity *1.B.2.b Natural Gas*,  
405  $38.2 \text{ kt CH}_4 \text{ yr}^{-1}$  for *1.B.2.c Venting and Flaring (oil, gas, combined oil and gas)* and  $10.4 \text{ kt yr}^{-1}$   
406  $^1$  for *1.B.2.a Oil* (UNFCCC, 2023b). This adds up to  $101.6 \text{ kt CH}_4 \text{ yr}^{-1}$ , about 3 times less than  
407 our estimate. Our estimate does not include emissions from infrastructure operated by other  
408 operators, for example the large gas production region in the Transylvanian Basin. An intensive  
409 ground-based study has been carried out there and the results are in preparation for publication  
410 (Jagoda et al., in preparation, 2024).

411 For comparison, we repeated the analysis using the EDGAR v7.0 inventory to estimate  
412 non-O&G sources for the large regions (see SI, Table S6). After removing double counting and  
413 adjusting for emissions from other sources as described previously, the total emissions  
414 measured attributed to O&G production are  $12,732 \pm 4,932 \text{ kg hr}^{-1}$ . This is slightly lower than  
415 the total emissions estimated using the TNO-CAMS v6.0 inventory  $13,200 \pm 4,932 \text{ kg hr}^{-1}$ ,  
416 indicating a larger fraction of non-O&G sources in the EDGAR v7.0 inventory. The inferred  
417 O&G emissions, taking into account the non-O&G emissions from the EDGAR inventory result

418 in a facility-weighted emission factor of  $5.1 \pm 2.0 \text{ kg hr}^{-1} \text{ site}^{-1}$ , consistent with the  $5.3 \pm 2.0 \text{ kg}$   
 419  $\text{hr}^{-1} \text{ site}^{-1}$  when using TNO-CAMS v6.0 for the non-O&G sectors. It is important to note that  
 420 the inventory estimates for the non-O&G sectors do not differ strongly between EDGAR v7.0  
 421 and TNO-CAMS v6.0 in the regions where we apply the corrections. However, this is not the  
 422 case for all regions in the southern Romanian production basin. Table S7 in the Supplement  
 423 shows that the discrepancies between the two inventories can become large. Specifically, in  
 424 EDGAR v7.0, the non-O&G emissions are higher than those in TNO-CAMS v6.0, nearly  
 425 double in some cases. Moreover, O&G emissions are very low in EDGAR, whereas they  
 426 contribute to almost half of the emissions in TNO-CAMS v6.0. Because of this more balanced  
 427 contribution from all sources, we use the estimates from TNO-CAMS v6.0 for our central  
 428 emission factor estimate and for the upscaling.

429 *Table 1 - Measured emission rates (ER) and estimates of the O&G related fraction of total CH<sub>4</sub>*  
 430 *emissions in target regions and clusters. “Non-O&G emissions (kg hr<sup>-1</sup>)” are extracted from*  
 431 *the TNO-CAMS v6.0 inventory for the target regions and are used to derive ERs from the O&G*  
 432 *industry in the area (“O&G emissions”). The last column shows the emission factor (kg CH<sub>4</sub>*  
 433 *hr<sup>-1</sup> site<sup>-1</sup>). Numbers in bold are used for upscaling to the national scale (see text for details).*

Flight ID	Target region/cluster	# facilities	# wells	Total Measured Emissions (kg hr <sup>-1</sup> )	Non-O&G emissions (kg hr <sup>-1</sup> )	O&G emissions (kg hr <sup>-1</sup> )	EF (kg h <sup>-1</sup> site <sup>-1</sup> )
SA01	R7	496	337	8517 ± 2097	1388	7129 ± 2097	14.4 ± 4.2
SA02	R7	504	343	8335 ± 1440	1388	6947 ± 1440	13.8 ± 2.9
SA03	R5a	827	654	4556 ± 2570	772	3784 ± 2570	4.6 ± 3.1
SA04	R5a-small	818	642	2920 ± 935	374	2516 ± 935	3.1 ± 1.1
SA05	R6C2C3C4	471	379	1729 ± 912	-	1729 ± 912	3.7 ± 1.9
SA06	R7C3C4	124	92	1481 ± 287	-	1481 ± 287	11.9 ± 2.3
SA07	R7C2	71	44	1395 ± 546	-	1395 ± 546	19.6 ± 7.7
SA08	R7VentArea	67	41	602 ± 209	-	602 ± 209	9.0 ± 3.1
SA09	R4C5	390	347	477 ± 106	-	477 ± 106	1.2 ± 0.3
SA10	R6C6	29	16	469 ± 170	130†	339 ± 170	11.7 ± 5.9
SA11	R7Vent	37	20	266 ± 113	-	266 ± 113	7.2 ± 3.1
SA12	R7C5	59	45	259 ± 47	-	259 ± 47	4.4 ± 0.8
SA13	R4C2C3	247	186	246 ± 89	-	246 ± 89	1.0 ± 0.4
SA14	R6C5	27	21	131 ± 85	-	131 ± 85	4.9 ± 3.1
SA16	R8C1	29	19	90 ± 49	-	90 ± 49	3.1 ± 1.7
SA17	R7C8	48	43	78 ± 101	-	78 ± 101	1.6 ± 2.1
SA18	R7C1Facility	8	5	13 ± 9	-	13 ± 9	1.6 ± 1.1
Weighted mean, everything		4358	3303	31667 ± 10039	*, †	27513 ± 9765	6.3 ± 2.2
No double counting		2516	1956		*, †, ††	<b>13200 ± 4932</b>	<b>5.3 ± 2.0</b>
Sum of clusters in R7		377	270			3828 ± 1199	10.2 ± 3.2
Only clusters with 100% fossil		1570	1238			6970 ± 2610	4.4 ± 1.7

\* considering the absolute non-O&G emissions from the TNO-CAMS inventory for the large regions and 100% O&G contribution for the clusters

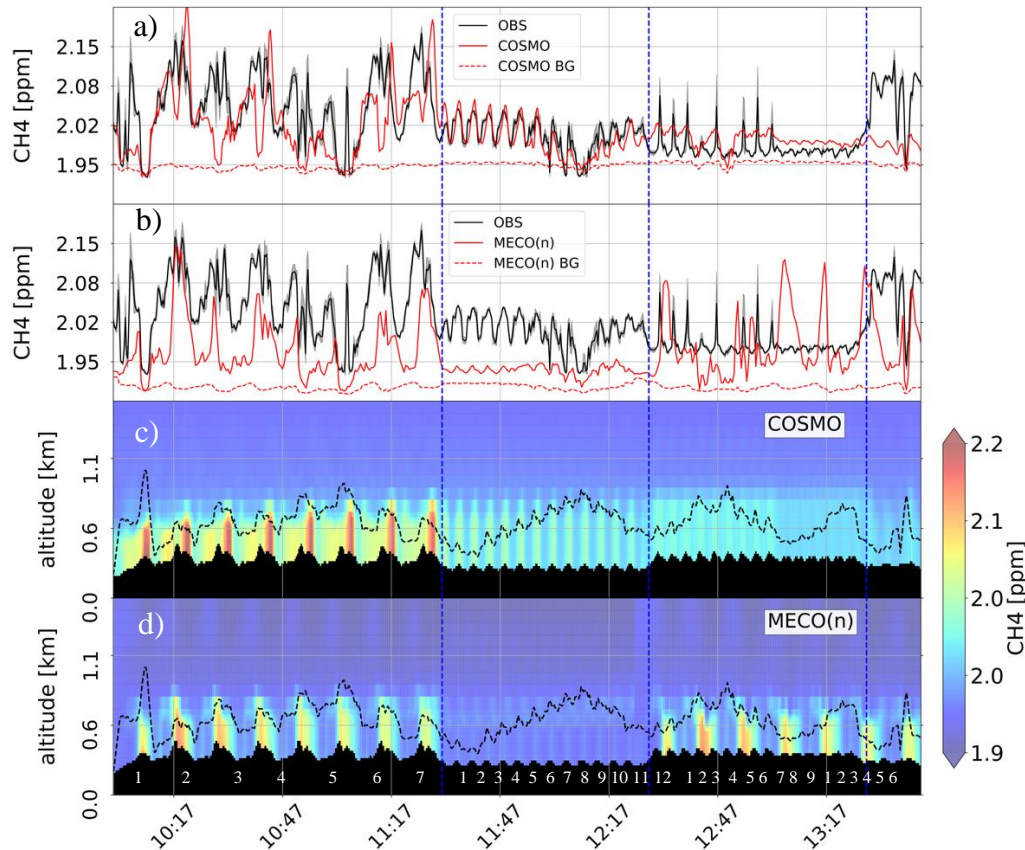
† accounting for landfill within R6C6

†† excluding cluster quantifications in R7

## 434 **3.2. Qualitative information from measurement - simulation comparisons**

### 435 **3.2.1. Example comparison of meteorology and CH<sub>4</sub> for a mass balance flight**

436 Figure 3 shows an example of a comparison between measurements along the SA mass  
437 balance flight from October 17, 2019, with results from the COSMO-GHG and MECO(3)  
438 models. The top two panels show simulated and measured CH<sub>4</sub> mole fractions along the flight  
439 track and the bottom two panel shows the vertical CH<sub>4</sub> profiles in the simulations along the  
440 flight track above the changing orography (black). During this flight, 4 different clusters and  
441 combinations of clusters were circled multiple times at different altitude; the flight altitude is  
442 included in the bottom panels as dashed black line. The repeating orographic patterns guide the  
443 eye in following the circular flight patterns around the clusters and are numbered in white. The  
444 colored contours illustrate the vertical CH<sub>4</sub> profiles along the flight track. The measured plume  
445 in the first, largest, cluster is captured relatively well by the simulation for some of the cycles,  
446 but during some cycles the flight track is partly above the boundary layer in the models and the  
447 peak is not fully captured. During cycles 4 and 5, the observations suggest that the aircraft was  
448 flying above the boundary layer also in reality, but one sharp, narrow peak was still observed  
449 after the highest orographic peak in the measurements, which is missing in the simulation. For  
450 the second cluster that was cycled 12 times, the COSMO-GHG model captures the plumes  
451 better than the MECO(3) model. For both models, the simulated and measured CH<sub>4</sub> mole  
452 fractions show a consistent transition out of the boundary layer in cycles 7-9, indicating a good  
453 representation of the boundary layer height in the models. For the third cluster, the models are  
454 missing the large, sharp peaks, indicating missing emissions in this cluster. In addition, the  
455 MECO(3) model simulates higher plumes when the flight track was in the model boundary  
456 layer, but lower plumes when the flight track was outside the boundary layer. For the last  
457 cluster, the simulated and measured elevations are small and relatively consistent for COSMO-  
458 GHG, but the MECO(3) model simulates some larger plumes spanning more than one cycle,  
459 indicating larger scale upwind contamination, which was also documented in the observations.



460  
 461 *Figure 3 – Measurements and simulation results of (a&b) CH<sub>4</sub> mole fraction along the flight*  
 462 *track, and (c&d) the vertical CH<sub>4</sub> profile along the flight track as simulated by the COSMO*  
 463 *model (a&c) and the MECO(3) model. Model background fields are shown as dashed lines in*  
 464 *a&b. Panel c&d also include the flight track as black dashed line, and the black contour at the*  
 465 *bottom shows the orography in this mountainous terrain; the repeating patterns illustrate*  
 466 *individual cycles around the clusters R6C2C3C4, R6C5, R6C6 and R6C7, cycles are numbered*  
 467 *in white. The flight around cluster R6C7 did not allow successful emission quantification*  
 468 *because of an upwind influence and is therefore not included in Table 1.*

469 A similar analysis was performed for each flight with the goal to identify plumes where either  
 470 the simulation results or the measurements indicated that the respective circle was flown outside  
 471 the simulated or actual boundary layer. In this case, the respective plume was not retained for  
 472 the measurement – simulation comparison. In total, 10 out of 200 individual plumes were  
 473 rejected this way. In addition, 66 circles around clusters that were influenced by signals from  
 474 upwind sources were excluded.

### 475 3.2.2. Model performance in terms of meteorology

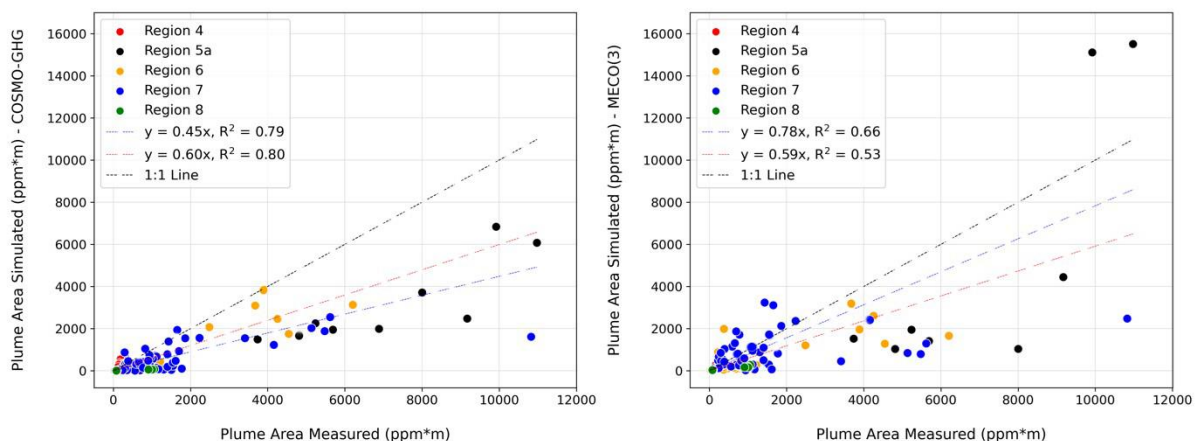
476 As mentioned above, the low winds during the campaign period presented difficult  
 477 meteorological conditions for emissions quantification. We performed a thorough  
 478 meteorological analysis to identify days when the meteorological conditions agree well between  
 479 the two models and the measurements. The results are shown in the Supplementary Information  
 480 S.1, which illustrate that it was not possible to identify days when the meteorological conditions  
 481 agree well between the two models and the measurements. Therefore, it was decided not to  
 482 focus on individual days or flights. Rather, in the following, we compare the measured and  
 483 simulated plume areas statistically across all available flights. This is done to investigate  
 484 whether correlation of measured and simulated CH<sub>4</sub> enhancements from the raster flights,

485 which cover a wider region, is similar to the one for the individual plumes quantified during the  
 486 mass balance flights. The analysis, which is described in the section below, can also possibly  
 487 identify regional differences and be used to derive approximate scaling factors for the raster  
 488 flights in comparison with the mass balance flights.

### 489 3.3. Measurement - model comparison of plume areas for mass balance flights

490 We first evaluate individual plume-level data from the mass balance flights, because for  
 491 these flights we have measured emission rates from the mass balance approach. Thus, we can  
 492 compare the measured and simulated plume areas and derive a correction factor for the emission  
 493 rates assumed in the model that would bring the measured and simulated plumes to agreement.  
 494 A total of 256 plumes were identified, 66 of them were rejected, and 190 plumes were retained  
 495 for analysis. Fig. 4 shows plume area comparison of these 190 plumes from the SA mass  
 496 balance flights and COSMO-GHG and MECO(3) models, respectively.

497 For mass balance flights around production clusters, each circle around a cluster results  
 498 in one or few down-wind plumes (which are integrated in our analysis), but for mass balance  
 499 flights targeting larger regions, numerous well-separated plumes can generally be quantified  
 500 from a single circle. The high scatter in the comparison between simulated and measured plume  
 501 areas can be ascribed to a number of factors, for example: i) large variability in actual emissions  
 502 from different source areas (here: production clusters), including the important role of super  
 503 emitters, ii) difficult meteorological conditions with low wind leading to variable plume  
 504 representations, both in the real atmosphere and in the model, iii) over- or underestimates  
 505 associated with the dynamics of the planetary boundary layer, and iv) variable measurement  
 506 distance from the emission points. The scatter in the comparison of plume areas with MECO(3)  
 507 results is even larger than for the COSMO-GHG model. This is ascribed to the fact that the  
 508 meteorological fields in COSMO-GHG are nudged to observations, whereas MECO(3) nudges  
 509 only the global model instance, implying more degrees of freedom within the nested instances  
 510 to develop their own (sub-synoptic) meteorological situation which might deviate from the data  
 511 used for nudging. Indeed, the meteorological evaluation (See Supplementary Information S.1)  
 512 shows that the meteorological fields in COSMO-GHG (directly nudged) are closer to the  
 513 observed meteorological parameters than for MECO(3), as expected.



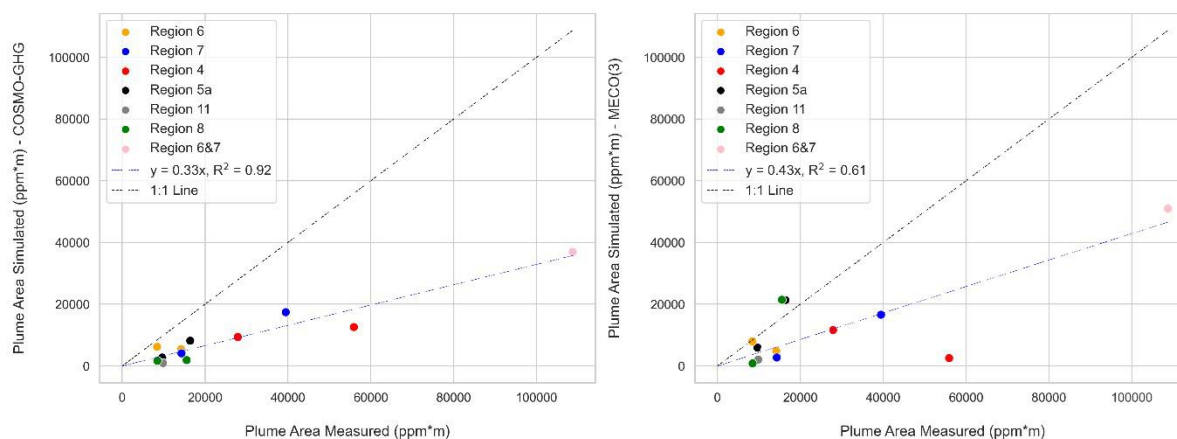
514  
 515 *Figure 4 - Comparisons between plume areas calculated from measurements and simulations*  
 516 *with COSMO-GHG (left) and MECO(3) (right). Blue dashed lines show linear fits to all data*  
 517 *and red dashed lines linear fits to the plumes from the clusters only, without the points from*  
 518 *the larger regions. Plots zooming in on the region of plume areas up to 2,000 ppm \* m are*  
 519 *shown Figure S1 in the SI.*

520 Nevertheless, despite the variability, it is evident that most of the points fall well below  
521 the 1:1 line, which means that the simulated plume areas along the flight track that were  
522 generated with an assumed emission factor of  $1 \text{ g s}^{-1} \text{ site}^{-1}$ , thus  $3.6 \text{ kg hr}^{-1} \text{ site}^{-1}$ , generally  
523 underestimate the measured plume areas. The further the points fall below the 1:1 line, the  
524 higher the implied mismatch in the emission rate that was assumed in the model. A linear fit to  
525 all the measured and simulated plumes has a slope of 0.44 for COSMO-GHG, and 0.78 for  
526 MECO(3). When we exclude the points from the larger regions, where the measured plumes  
527 are often further away from the source regions, the slopes change slightly to 0.56 for COSMO-  
528 GHG, and to 0.62 for MECO(3). This suggests that the assumed emission rate in the model is  
529 on average underestimated by about a factor of 2. However, quantitative interpretation is  
530 problematic in this approach, since the slope of the linear fit is largely determined by a relatively  
531 small number of plumes with large plume areas. Furthermore, the sampling is biased towards  
532 clusters where more circles were flown (i.e., circles at more altitude levels), and does not  
533 consider the number of facilities per cluster. In addition, there may be systematic biases in the  
534 models, e.g. due to model resolution or meteorological conditions (as discussed above), that  
535 lead to smaller plume areas in the models compared to the measurements. For the present  
536 purpose, we will compare the slope of observed and simulated plume areas from the mass  
537 balance flights determined here with the slope of observed and simulated  $\text{CH}_4$  enhancements  
538 from the raster flights in section 3.4.2 to investigate whether the enhancements observed during  
539 the raster flights qualitatively agree with the ones from the mass balance flights.

#### 540 **3.4. Measurement - model comparison of plume areas for raster flights**

541 Figure 5 shows the comparison of the integrated enhancement above background along  
542 the flight tracks for  $\text{CH}_4$  mole fractions measured during the raster flights and simulated with  
543 the two models. The scatter for these integrated enhancements is smaller than for the individual  
544 plume areas shown in Fig 4., which likely reflects the fact that the integrated enhancements are  
545 the sum of numerous plumes, and high and low values average out for the integrated  
546 enhancements.

547 Similar to the plume area comparison from the mass balance flights (Fig. 4), most of the  
548 points fall below the 1: 1 line, again indicating that the emission rate of  $3.6 \text{ kg hr}^{-1} \text{ site}^{-1}$  assumed  
549 in the models is insufficient to explain the observed concentrations. The slopes of the  
550 orthogonal linear regressions of 0.43 and 0.33 for the two different models are even lower than  
551 for the mass balance flights above, indicating a possible underestimate by up to a factor of 3 in  
552 the assumed emission rate. Still, the slopes are in a similar range as the slopes from the mass  
553 balance flights in Fig. 4. It is important to note that these slopes were now derived from the  
554 simulated fields under similar conditions as the ones for the individual plumes from the clusters.  
555 Thus, whereas various factors could cause systematic under- or overestimates in simulated  
556 versus measured  $\text{CH}_4$  enhancements, the similar slopes obtained for the two types of flights  
557 suggest that the emission characteristics of the plumes observed during the mass balance and  
558 raster flights are compatible. Thus, the emission factors derived for a limited number of clusters  
559 in section 3.3 are likely representative for the larger areas covered in the mass balance flights,  
560 and thus for a large fraction of the Southern Romanian O&G production infrastructure. We  
561 conclude that the  $\text{CH}_4$  enhancements observed on the BN2 aircraft during the raster flights  
562 generally support the emission factors derived in section 3.1 from the mass balance approach.



563  
564

565 *Figure 5 - Comparison between integrated CH<sub>4</sub> enhancements from measurements during*  
 566 *raster flights on the BN2 aircraft, and simulations along the flight tracks with COSMO-*  
 567 *GHG (left) and MECO(3) (right). Different colors represent different regions. Linear fits to*  
 568 *the data are shown as blue dashed lines and the 1: 1 line is shown as black dashed line.*

#### 569 4. Conclusions

570 Airborne measurements of methane performed from two aircraft during the ROMEO  
 571 2019 campaign were evaluated to obtain emission rate estimates representative for production  
 572 clusters and larger regions in the O&G production basin in Southern Romania. Emissions  
 573 determined from a mass balance approach yield a wide range of instantaneous emission factor  
 574 estimates between different clusters, supporting the heterogeneity of emissions across  
 575 individual sites, regions and time. Assessment of the O&G emissions from flights around larger  
 576 regions is difficult because of the unknown contribution of emissions from other sectors. From  
 577 mass balance estimates covering a total of 2,516 sites, using the TNO-CAMS inventory to  
 578 derive emissions from non-O&G sources for the large regions, and assuming 100% of the  
 579 observed emissions in the smaller clusters to originate from O&G production, we derive total  
 580 emissions of  $13,200 \pm 4,932 \text{ kg hr}^{-1}$  for the covered regions in Southern Romania. This results  
 581 in a facility-weighted emission factor of  $5.3 \pm 2.0 \text{ kg hr}^{-1} \text{ site}^{-1}$ , consistent with the previously  
 582 published estimate from ground-based quantifications of  $5.4 \text{ kg hr}^{-1} \text{ oil production site}^{-1}$  (range  
 583  $3.6 - 8.4 \text{ kg hr}^{-1} \text{ site}^{-1}$ , (Stavropoulou et al., 2023). The facility-weighted average for 1,570  
 584 facilities in dense production clusters, where we are certain that the dominant contribution is  
 585 from the O&G infrastructure is  $4.4 \pm 1.7 \text{ kg hr}^{-1} \text{ site}^{-1}$ , aligning with the estimate from larger  
 586 regions. Using the EF of  $5.3 \text{ kg hr}^{-1} \text{ site}^{-1}$  to scale up to the national scale results in an annual  
 587 emission rate estimate of  $344 \pm 130 \text{ ktons CH}_4 \text{ yr}^{-1}$ , which is about three times higher than the  
 588 UNFCCC reported national emissions from the O&G industry for Romania. Mole fraction  
 589 measurements carried out in raster flight tracks over wider areas lacked meteorological  
 590 measurements and therefore could not be used to derive direct estimates of emission rates. To  
 591 support the evaluation, simulations with two numerical atmospheric models were carried out  
 592 and the simulated CH<sub>4</sub> fields were compared with the measurements. Due to the difficult  
 593 meteorological conditions, direct quantitative evaluation remains challenging, but the  
 594 comparison of observed and simulated enhancements consistently suggests that the prior  
 595 emission rate of  $3.6 \text{ kg hr}^{-1} \text{ site}^{-1}$  used in the models is too low. In addition, the correlation of  
 596 measured and simulated CH<sub>4</sub> enhancements for the raster flights over larger areas is consistent  
 597 with the correlations observed in mass balance flights around well-defined production clusters,  
 598 indicating the validity of the derived emission factors for a large part of the southern Romanian  
 599 O&G production region. Airborne measurements for the regions and clusters, where ground-



600 based surveys can be also applied, can provide important additional insight, such as: (I) the  
601 influence of super emitters is included as a realistic fraction in the total airborne measured  
602 emissions while super emitters may be either missed or accidentally be overrepresented in  
603 ground surveys, (II) the influence of non-O&G sources on total emission can be studied, and  
604 (III) airborne quantification can cover large areas in a much shorter time compared to ground-  
605 based quantification. We conclude that the top-down emission estimates derived here from  
606 airborne surveys over larger regions support the previously published emission rate estimates  
607 derived from ground-based bottom-up quantifications during the ROMEO 2019 campaign.  
608 These results confirm that O&G methane emissions in 2019 were much higher than reported to  
609 UNFCCC and estimated in EDGAR within our study domain.

610 **Data availability.** In-situ measurements and outputs of model simulations along flight tracks  
611 are available from Maazallahi et al. (2024a).

612 **Code availability.** MATLAB® codes for investigation of in-situ measurements from circular-  
613 pattern and raster flights and outputs of model simulations are available from Maazallahi et al.  
614 (2024b).

615 **Acknowledgements.** The ROMEO project was supported by the Climate and Clean Air  
616 Coalition (CCAC) Oil and Gas Methane Science Studies (MMS) hosted by the United Nations  
617 Environment Programme UNEP. Funding was provided by the Environmental Defense Fund,  
618 Oil and Gas Climate Initiative, European Commission, and CCAC. This project received  
619 further support from the H2020 Marie Skłodowska-Curie project Methane goes Mobile –  
620 Measurements and Modelling (MEMO<sup>2</sup>; <https://h2020-memo2.eu/>), grant number 722479. The  
621 modeling work used resources of the Deutsches Klimarechenzentrum (DKRZ) granted by its  
622 Scientific Steering Committee (WLA) under project ID bd0617 to perform the MECO(3)  
623 simulations.

624 **Competing interests.** At least one of the (co-) authors is a member of the editorial board of  
625 Atmospheric Chemistry and Physics. The authors have no other competing interests to declare.

626 **Author contributions.** MLS, SAC, SG, AP, and MA, carried out and evaluated airborne  
627 measurements, HM carried out the quantitative data evaluation, SJS carried out the  
628 meteorological analysis, FS supported the data analysis, MS, DB, MM, PJ, carried out the  
629 atmospheric simulations, AV, HDvdG, SD, and NVS provided inventory information, SS, MA,  
630 AC and TR designed and planned the study, HM and TR drafted the manuscript.

## 631 **References**

- 632 Allen, D. T., Torres, V. M., Thomas, J., Sullivan, D. W., Harrison, M., et al.: Measurements of  
633 methane emissions at natural gas production sites in the United States, Proc. Natl. Acad.  
634 Sci. U. S. A., 110, 17768-17773, 10.1073/pnas.1304880110, 2013.
- 635 Alvarez, R. A., Zavala-Araiza, D., Lyon, D. R., Allen, D. T., Barkley, Z. R., et al.: Assessment of  
636 methane emissions from the US oil and gas supply chain, Science, 361, 186-188,  
637 10.1126/science.aar7204, 2018.
- 638 Baldauf, M., Seifert, A., Förstner, J., Majewski, D., Raschendorfer, M., et al.: Operational  
639 Convective-Scale Numerical Weather Prediction with the COSMO Model: Description and  
640 Sensitivities, Monthly Weather Review, 139, 3887-3905, [https://doi.org/10.1175/MWR-D-](https://doi.org/10.1175/MWR-D-10-05013.1)  
641 [10-05013.1](https://doi.org/10.1175/MWR-D-10-05013.1), 2011.

642 Brandt, A. R., Heath, G. A., Kort, E. A., O'Sullivan, F., Pétron, G., et al.: Methane Leaks from  
643 North American Natural Gas Systems, *Science*, 343, 733-735,  
644 doi:10.1126/science.1247045, 2014.

645 Brunner, D., Kuhlmann, G., Marshall, J., Clément, V., Fuhrer, O., et al.: Accounting for the  
646 vertical distribution of emissions in atmospheric CO<sub>2</sub> simulations, *Atmos. Chem. Phys.*, 19,  
647 4541-4559, 10.5194/acp-19-4541-2019, 2019.

648 Collins, W. J., Webber, C. P., Cox, P. M., Huntingford, C., Lowe, J., et al.: Increased importance  
649 of methane reduction for a 1.5 degree target, *Environmental Research Letters*, 13, 054003,  
650 10.1088/1748-9326/aab89c, 2018.

651 Conley, S., Faloon, I., Mehrotra, S., Suard, M., Lenschow, D. H., et al.: Application of Gauss's  
652 theorem to quantify localized surface emissions from airborne measurements of wind and  
653 trace gases, *Atmos. Meas. Tech.*, 10, 3345-3358, 10.5194/amt-10-3345-2017, 2017.

654 Delre, A., Hensen, A., Velzeboer, I., van den Bulk, P., Edjabou, M. E., et al.: Methane and  
655 ethane emission quantifications from onshore oil and gas sites in Romania, using a tracer  
656 gas dispersion method, *Elementa: Science of the Anthropocene*, 10,  
657 10.1525/elementa.2021.000111, 2022.

658 Denier van der Gon, H. A. C., Kuenen, J., Boleti, E., Muntean, M., Maenhout, G., et al.:  
659 Emissions and natural fluxes Dataset, available from: [https://www.che-](https://www.che-project.eu/sites/default/files/2019-01/CHE-D2-3-V1-0.pdf)  
660 [project.eu/sites/default/files/2019-01/CHE-D2-3-V1-0.pdf](https://www.che-project.eu/sites/default/files/2019-01/CHE-D2-3-V1-0.pdf), (last access: 06 Dec. 2023),  
661 2018., 2018.

662 E-PRTR: European Industrial Emissions Portal. Available from:  
663 <https://industry.eea.europa.eu/explore/explore-by-pollutant>, last access 06 Dec. 2023.,  
664 2023.

665 EDGAR: Emissions Database for Global Atmospheric Research. Available from:  
666 <https://edgar.jrc.ec.europa.eu/>, last access: 06 Dec. 2023, 2023.

667 European-Commission: Deal on first-ever EU law to curb methane emissions,  
668 [https://ec.europa.eu/commission/presscorner/detail/en/IP\\_23\\_5776](https://ec.europa.eu/commission/presscorner/detail/en/IP_23_5776), 2023.

669 Fernandez, J. M., Maazallahi, H., France, J. L., Menoud, M., Corbu, M., et al.: Street-level  
670 methane emissions of Bucharest, Romania and the dominance of urban wastewater,  
671 *Atmospheric Environment: X*, 13, 100153, <https://doi.org/10.1016/j.aeaoa.2022.100153>,  
672 2022.

673 Gonzalez Moguel, R., Vogel, F., Ars, S., Schaefer, H., Turnbull, J. C., et al.: Using carbon-14 and  
674 carbon-13 measurements for source attribution of atmospheric methane in the Athabasca  
675 oil sands region, *Atmos. Chem. Phys.*, 22, 2121-2133, 10.5194/acp-22-2121-2022, 2022.

676 Gupta, H. V., Kling, H., Yilmaz, K. K., and Martinez, G. F.: Decomposition of the mean squared  
677 error and NSE performance criteria: Implications for improving hydrological modelling,  
678 *Journal of Hydrology*, 377, 80-91, <https://doi.org/10.1016/j.jhydrol.2009.08.003>, 2009.

679 Harriss, R., Alvarez, R. A., Lyon, D., Zavala-Araiza, D., Nelson, D., et al.: Using Multi-Scale  
680 Measurements to Improve Methane Emission Estimates from Oil and Gas Operations in  
681 the Barnett Shale Region, Texas, *Environmental Science & Technology*, 49, 7524-7526,  
682 10.1021/acs.est.5b02305, 2015.

683 Hersbach, H., Bell, B., Berrisford, P., Biavati, G., Horányi, A., et al.: ERA5 hourly data on single  
684 levels from 1940 to present, Copernicus Climate Change Service (C3S) Climate Data Store  
685 (CDS), DOI: 10.24381/cds.adbb2d47, last access 06 Dec. 2023, 2023.

686 IEA: Global Methane Tracker 2022, [https://www.iea.org/reports/global-methane-tracker-](https://www.iea.org/reports/global-methane-tracker-2022)  
687 [2022](https://www.iea.org/reports/global-methane-tracker-2022), last access: 2 November 2022., 2023.

688 Jähn, M., Kuhlmann, G., Mu, Q., Haussaire, J. M., Ochsner, D., et al.: An online emission  
689 module for atmospheric chemistry transport models: implementation in COSMO-GHG  
690 v5.6a and COSMO-ART v5.1-3.1, *Geosci. Model Dev.*, 13, 2379-2392, 10.5194/gmd-13-  
691 2379-2020, 2020.

692 Johnson, M. R., Tyner, D. R., Conley, S., Schwietzke, S., and Zavala-Araiza, D.: Comparisons of  
693 Airborne Measurements and Inventory Estimates of Methane Emissions in the Alberta  
694 Upstream Oil and Gas Sector, *Environmental Science & Technology*, 51, 13008-13017,  
695 10.1021/acs.est.7b03525, 2017.

696 Kerkweg, A., and Jöckel, P.: The 1-way on-line coupled atmospheric chemistry model system  
697 MECO(n) – Part 1: Description of the limited-area atmospheric chemistry model  
698 COSMO/MESSy, *Geosci. Model Dev.*, 5, 87-110, 10.5194/gmd-5-87-2012, 2012.

699 Klausner, T., Mertens, M., Huntrieser, H., Galkowski, M., Kuhlmann, G., et al.: Urban  
700 greenhouse gas emissions from the Berlin area: A case study using airborne CO<sub>2</sub> and CH<sub>4</sub>  
701 in situ observations in summer 2018, *Elementa: Science of the Anthropocene*, 8,  
702 10.1525/elementa.411, 2020.

703 Knoben, W. J. M., Freer, J. E., and Woods, R. A.: Technical note: Inherent benchmark or not?  
704 Comparing Nash–Sutcliffe and Kling–Gupta efficiency scores, *Hydrol. Earth Syst. Sci.*, 23,  
705 4323-4331, 10.5194/hess-23-4323-2019, 2019.

706 Korbeň, P., Jagoda, P., Maazallahi, H., Kammerer, J., Nečki, J. M., et al.: Quantification of  
707 methane emission rate from oil and gas wells in Romania using ground-based  
708 measurement techniques, *Elementa: Science of the Anthropocene*, 10,  
709 10.1525/elementa.2022.00070, 2022.

710 Kuenen, J., Dellaert, S., Visschedijk, A., Jalkanen, J.-P., Super, I., and Denier van der Gon, H.:  
711 CAMS-REG-v4: a state-of-the-art high-resolution European emission inventory for air  
712 quality modelling, *Earth Syst. Sci. Data*, 14, 491–515, [https://doi.org/10.5194/essd-14-491-](https://doi.org/10.5194/essd-14-491-2022)  
713 2022, 2022.

714 Lee, Y., and Deming, D.: Evaluation of thermal conductivity temperature corrections applied  
715 in terrestrial heat flow studies, *Journal of Geophysical Research: Solid Earth*, 103, 2447-  
716 2454, <https://doi.org/10.1029/97JB03104>, 1998.

717 Lopez, M., Sherwood, O. A., Dlugokencky, E. J., Kessler, R., Giroux, L., et al.: Isotopic signatures  
718 of anthropogenic CH<sub>4</sub> sources in Alberta, Canada, *Atmos. Environ.*, 164, 280-288,  
719 <https://doi.org/10.1016/j.atmosenv.2017.06.021>, 2017.

720 Lu, X., Harris, S. J., Fisher, R. E., France, J. L., Nisbet, E. G., et al.: Isotopic Signatures of Major  
721 Methane Sources in the Coal Seam Gas Fields and Adjacent Agricultural Districts,  
722 Queensland, Australia, *Atmos. Chem. Phys*, 2021, 1-36, 10.5194/acp-2021-76, 2021.

723 Maasackers, J. D., Jacob, D. J., Sulprizio, M. P., Turner, A. J., Weitz, M., Wirth, T., Hight, C.,  
724 DeFigueiredo, M., Desai, M., Schmeltz, R., Hockstad, L., Bloom, A. A., Bowman, K. W.,  
725 Jeong, S., and Fischer, M. L.: Gridded National Inventory of U.S. Methane Emissions,  
726 *Environ. Sci. Technol.*, 50, 13123–13133, <https://doi.org/10.1021/acs.est.6b02878>, 2016.

727 Maazallahi, H., Stavropoulou, F., Sutanto, S. J., Steiner, M., Brunner, D., Mertens, M., Jöckel,  
728 P., Visschedijk, A., Denier van der Gon, H., Dellaert, S., Velandia Salinas, N., Schwietzke, S.,  
729 Zavala-Araiza, D., Ghemulet, S., Pana, A., Ardelean, M., Corbu, M., Calcan, A., Conley, S. A.,  
730 Smith, M. L., Röckmann, T.: Data for Airborne in-situ quantification of methane emissions  
731 from oil and gas production in Romania, Integrated Carbon Observation System (ICOS)  
732 [data set], [https://fileshare.icos-cp.eu/apps/files/?dir=/ROME0\\_Flight&fileid=3286570](https://fileshare.icos-cp.eu/apps/files/?dir=/ROME0_Flight&fileid=3286570),  
733 2024a.

734 Maazallahi, H., Stavropoulou, F., Sutanto, S. J., Steiner, M., Brunner, D., Mertens, M., Jöckel,  
735 P., Visschedijk, A., Denier van der Gon, H., Dellaert, S., Velandia Salinas, N., Schwietzke, S.,  
736 Zavala-Araiza, D., Ghemulet, S., Pana, A., Ardelean, M., Corbu, M., Calcan, A., Conley, S. A.,  
737 Smith, M. L., Röckmann, T.: MATLAB® code for evaluation of airborne in-situ  
738 measurements and model simulations, Zenodo, [code],  
739 <https://doi.org/10.5281/zenodo.12701604>, 2024b.

740 Maazallahi, H., Fernandez, J. M., Menoud, M., Zavala-Araiza, D., Weller, Z. D., et al.: Methane  
741 mapping, emission quantification, and attribution in two European cities: Utrecht (NL) and  
742 Hamburg (DE), *Atmos. Chem. Phys.*, 20, 14717-14740, 10.5194/acp-20-14717-2020, 2020.

743 Menoud, M., van der Veen, C., Necki, J., Bartyzel, J., Szénási, B., et al.: Methane (CH<sub>4</sub>) sources  
744 in Krakow, Poland: insights from isotope analysis, *Atmos. Chem. Phys.*, 2021, 13167–  
745 13185, 10.5194/acp-21-13167-2021, 2021.

746 Menoud, M., van der Veen, C., Maazallahi, H., Hensen, A., Velzeboer, I., et al.: CH<sub>4</sub> isotopic  
747 signatures of emissions from oil and gas extraction sites in Romania, *Elementa: Science of  
748 the Anthropocene*, 10, 10.1525/elementa.2021.00092, 2022.

749 Mielke-Maday, I., Schwietzke, S., Yacovitch, T. I., Miller, B., Conley, S., et al.: Methane source  
750 attribution in a U.S. dry gas basin using spatial patterns of ground and airborne ethane and  
751 methane measurements, *Elementa: Science of the Anthropocene*, 7,  
752 10.1525/elementa.351, 2019.

753 Nash, J. E., and Sutcliffe, J. V.: River flow forecasting through conceptual models part I — A  
754 discussion of principles, *J. Hydrol.*, 10, 282-290, [https://doi.org/10.1016/0022-  
755 1694\(70\)90255-6](https://doi.org/10.1016/0022-1694(70)90255-6), 1970.

756 Nickl, A. L., Mertens, M., Roiger, A., Fix, A., Amediak, A., et al.: Hindcasting and forecasting of  
757 regional methane from coal mine emissions in the Upper Silesian Coal Basin using the  
758 online nested global regional chemistry–climate model MECO(n) (MESSy v2.53), *Geosci.  
759 Model Dev.*, 13, 1925-1943, 10.5194/gmd-13-1925-2020, 2020.

760 Nisbet, E. G., Fisher, R. E., Lowry, D., France, J. L., Allen, G., et al.: Methane Mitigation:  
761 Methods to Reduce Emissions, on the Path to the Paris Agreement, *Reviews of Geophysics*,  
762 58, 2020.

763 Röckmann, T., Eyer, S., van der Veen, C., Popa, M. E., Tuzson, B., et al.: In situ observations of  
764 the isotopic composition of methane at the Cabauw tall tower site, *Atmos. Chem. Phys.*,  
765 16, 10469-10487, 10.5194/acp-16-10469-2016, 2016.

766 Saarnio, S., Winiwarter, W., and Leitão, J.: Methane release from wetlands and watercourses  
767 in Europe, *Atmos. Environ.*, 43, 1421-1429,  
768 <https://doi.org/10.1016/j.atmosenv.2008.04.007>, 2009.

769 Saunio, M., Stavert, A. R., Poulter, B., Bousquet, P., Canadell, J. G., et al.: The Global Methane  
770 Budget 2000-2017, *Earth Syst Sci Data*, 12, 1561-1623, 10.5194/essd-12-1561-2020, 2020.

771 Scarpelli, T. R., Jacob, D. J., Maasackers, J. D., Sulprizio, M. P., Sheng, J.-X., Rose, K., Romeo,  
772 L., Worden, J. R., and Janssens-Maenhout, G.: A global gridded (0.1° × 0.1°) inventory of  
773 methane emissions from oil, gas, and coal exploitation based on national reports to the  
774 United Nations Framework Convention on Climate Change, *Earth Syst. Sci. Data*, 12, 563–  
775 575, <https://doi.org/10.5194/essd-12-563-2020>, 2020.

776 Sheng, J.-X., Jacob, D. J., Maasackers, J. D., Sulprizio, M. P., Zavala-Araiza, D., and Hamburg, S.  
777 P.: A high-resolution (0.1° × 0.1°) inventory of methane emissions from Canadian and  
778 Mexican oil and gas systems, *Atmos. Environ.*, 158, 211–215,  
779 <https://doi.org/10.1016/j.atmosenv.2017.02.036>, 2017.

780 Shindell, D., Ravishankara, A. R., Kuylenstierna, J. C. I., Michalopoulou, E., Höglund-Isaksson,  
781 L., et al.: Global Methane Assessment: Benefits and Costs of Mitigating Methane Emissions,  
782 United Nations Environment Programme and Climate and Clean Air Coalition, Nairobi:  
783 United Nations Environment Programme., 2021.

784 Stavropoulou, F., Vinković, K., Kers, B., de Vries, M., van Heuven, S., et al.: High potential for  
785 CH<sub>4</sub> emission mitigation from oil infrastructure in one of EU's major production regions,  
786 Atmos. Chem. Phys., 23, 10399-10412, 10.5194/acp-23-10399-2023, 2023.

787 Szopa, S., Naik, V., Adhikary, B., Artaxo, P., Berntsen, T., et al.: Short-lived Climate Forcers, in:  
788 Climate Change 2021 – The Physical Science Basis: Working Group I Contribution to the  
789 Sixth Assessment Report of the Intergovernmental Panel on Climate Change, edited by:  
790 Intergovernmental Panel on Climate, C., Cambridge University Press, Cambridge, 817-922,  
791 2021.

792 UNFCCC: Paris Agreement to the United Nations Framework Convention on Climate Change,  
793 T.I.A.S. No. 16-1104, 2015.

794 UNFCCC: Greenhouse Gas Inventory Data—Comparison by Gas.  
795 [https://di.unfccc.int/comparison\\_by\\_gas](https://di.unfccc.int/comparison_by_gas), 2023., 2023a.

796 UNFCCC, Romania. 2023 Common Reporting Format (CRF) Table,  
797 <https://unfccc.int/documents/627660> 2023b

798 Weller, Z. D., Hamburg, S. P., and von Fischer, J. C.: A National Estimate of Methane Leakage  
799 from Pipeline Mains in Natural Gas Local Distribution Systems, Environmental Science &  
800 Technology, 54, 8958-8967, 10.1021/acs.est.0c00437, 2020.

801 Winterstein, F., and Jöckel, P.: Methane chemistry in a nutshell – the new submodels CH4  
802 (v1.0) and TRSYNC (v1.0) in MESSy (v2.54.0), Geosci. Model Dev., 14, 661-674,  
803 10.5194/gmd-14-661-2021, 2021.

804